Simulation of Unstart in Hypersonic Flow With a Dual-Mode Scramjet Model

Ian A. Hall[1] and Jonathan Poggie[2]
Purdue University, West Lafayette, IN, 47907-2045, USA

A validated model of hypersonic unstart will prove a valuable tool in diagnosing scramjet design issues and may provide a possible path towards preventing an unstart event in a scramjet. To this end, a computational model of an inlet-isolator was developed to study unstart. This model was compared to experimental data from the UT Austin Mach 5 Wind Tunnel and was shown to accurately reproduce both the fully started and unstarted inlet-isolator flowfields. The use of a body force rather than a moving mesh to initiate unstart is demonstrated, greatly reducing computational complexity to demonstrate unstart. The unstart shock and boundary layer interactions within this model are explored throughout the duration of the unstart process. Precursors to unstart are explored, specifically the wall pressures within the boundary layer, as the unstart system progresses upstream from its source.

I. Nomenclature

M	= Mach number
T_0	= Total Temperature
P_0	= Total Pressure
T_∞	= Freestream Static Temperature
P_∞	= Freestream Static Pressure
V_∞	= Freestream Velocity
γ	= Specific Heat Ratio
C_f	= Skin Friction Coefficient
$C_{f\text{-}RICH}$	= Grid Independent Skin Friction Coefficient
P_{RICH}	= Grid Independent Pressure
x	= Horizontal Position
y	= Vertical Position
h	= Isolator Height
ρ	= Density
ρu	= x Momentum
ρv	= y Momentum
ρe	= Energy
U	= x Velocity
V	= y Velocity
δ	= 99% Boundary Layer Thickness

II. Introduction

High-speed propulsion, specifically for supersonic and hypersonic vehicles, is a growing field of research of great national and international interest. Ramjet and scramjet propulsion systems, in particular, hold great promise for supersonic and hypersonic cruise vehicles, with the potential to unlock everything from first-strike military capabilities, to rapid intercontinental flight, to single-stage-to-orbit vehicles. However, to achieve true sustained hypersonic flight, numerous technological barriers still exist [1]. In particular, there exists a need for a deeper understanding of the aerodynamic characteristics of ramjet and scramjet propulsion systems in order to achieve stable flight.

Ramjets typically operate from Mach 2 to Mach 4.5 and, in the hypersonic regime, scramjets operate from around Mach 4 to Mach 20 [2]. While this transition of the vehicle's speed from supersonic to hypersonic is marked by large increases in heating and turbulence surrounding the vehicle, another important phenomenon is occurring within the propulsion system itself. The flow coming through the air intake in a ramjet is slowed to subsonic speeds by a shock train before it reaches the combustor. However, as the vehicle transitions to hypersonic speeds, the required length of

[1]Graduate Student, School of Aeronautics and Astronautics. Student Member AIAA.
[2]Associate Professor, School of Aeronautics and Astronautics. Associate Fellow AIAA.

the shock train becomes so long and static temperatures become so high that it is no longer feasible to slow the flow to subsonic speeds before it reaches the combustor. Thus, in a scramjet, as the vehicle's speed increases, the internal airflow moves into the supersonic regime, generating immense amounts of turbulence which introduces large amounts of variability in the combustion conditions [3]. In order to achieve true hypersonic cruise, assuming the vehicle had a rocket or gas-turbine engine to reach supersonic speeds, a vehicle would require both ramjet and scramjet propulsion. To this end, the dual-mode scramjet design was proposed in 1964 [3]. It is a propulsion system that can function as both a ramjet and a scramjet. It is capable of working in the intermediate flow range, with internal airflow entering the combustor at subsonic, transonic, and supersonic speeds.

Unfortunately, the extreme turbulence and unsteadiness inside dual-mode scramjet propulsion systems commonly leads to unstart and a catastrophic loss of propulsion. In unstart, the shock train captured within the isolator is pushed upstream and expelled out the inlet, which causes the airflow to the combustor to momentarily cut off as the air is forced out the inlet. This sudden loss of thrust can be caused be a variety of circumstances, such as combustion instabilities and freestrean variations (caused by changed inlet conditions). Regardless of what initiates it, however, the effect is catastrophic to flight [4]. This paper attempts to better understand dual-mode scramjet unstart so that a means to predict and mitigate this unstart can be developed.

In order to better understand unstart propagation in an inlet-isolator model, a high-fidelity CFD model needs to be created. In this paper, a computational model has been developed to study unstart, and it is compared to an experimental model developed by researchers at UT Austin. The accuracy of the computational model is studied to gain an understanding of its predictive capability and validate it for future computational studies.

III. Experimental Framework

Researchers at UT Austin (Wagner, Clemens, et al.) have developed an inlet-isolator test section model that can initiate unstart, mounted in a Mach 5 wind tunnel, so that they may investigate hypersonic unstart [5-8]. In the course of running extensive experiments, they have demonstrated repeatable unstart using a ramp that disrupts a fully started flow at the exit of the isolator. They found that raising a ramp at the outlet of an inlet-isolator model could induce unstart, mimicking the effect of a flow blockage from the combustor. This flow blockage represents a sudden pressure rise in the combustor section that disrupts the shock train and initiates unstart. Once the ramp is raised to a critical angle, a high-pressure shock is initiated, which begins propagating upstream towards the inlet, obliterating the standing oblique shock train in the isolator. This pushes the air in the isolator channel upstream and out of the inlet [5].

The referenced experiments studied a number of different inlet-isolator model variations, as well as different ramp deployment angles and times. For the purposes of this paper the chosen configuration is a 6 degree inlet ramp. This was chosen because it was the most studied of the different models. In their experiments, Wagner et al. measured the freestream total temperature to be $T_0 = 328$ K, total pressure to be $P_0 = 2.465$ MPa, and incoming Mach number to be $M = 4.9$.

Using the isentropic flow relations (Eqs. 1, 2, and 3) the static freestream conditions come to $T_\infty = 56.53$ K, $P_\infty = 5.240$ kPa, and $V_\infty = 738.5$ m/s. Note that this assumes a specific heat ratio of $\gamma = 1.4$. This matches with what Wagner gives for the calculated freestream conditions in Appendix D of his thesis [7]: $T_\infty = 56$ K, $P_\infty = 5.38$ kPa, and $V_\infty = 740$ m/s.

$$T_\infty = \frac{T_0}{\left(1+\frac{(\gamma-1)}{2}M^2\right)} \tag{1}$$

$$P_\infty = \frac{P_0}{\left(1+\frac{(\gamma-1)}{2}M^2\right)^{\frac{\gamma}{\gamma-1}}} \tag{2}$$

$$V_\infty = M\sqrt{\gamma R T_\infty} \tag{3}$$

The geometry of the experimental inlet-isolator model tested is a rectangular channel with a 6 degree inlet ramp on the roof for roughly the first third of the channel. The total channel length is 333 mm long, measuring 25.4 mm high for the rectangular cross-section portion, known as the isolator. This section is 242.3mm in length, whereas the inlet section with the 6 degree ramp is 90.7 mm long. The width of the channel is twice the isolator height, measuring 50.8 mm, but the calculations completed for this paper neglected this, as they were all 2D. The geometry has been reproduced in Fig. 1. Note that the units are in meters in this figure.

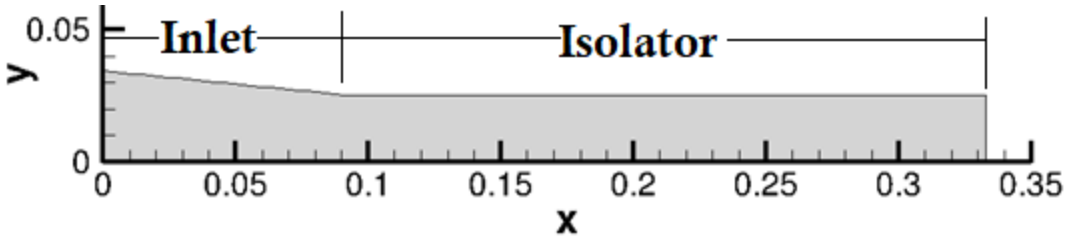

Fig. 1 Inlet-Isolator Test Section (axes in m)

It is important to note that the test section was mounted directly on the floor of the UT Austin wind tunnel, so a thick boundary layer developed before the flow entered the test section. The boundary layer thickness, measured as where the flow velocity was up to 99% of the freestream velocity, was 19.3 mm. This is over half of the height of the inlet so it had a significant effect on the internal flow. Note that the boundary layer on the roof of the inlet-isolator test section developed only from a sharp leading edge.

In order to initiate unstart, the researchers at UT Austin used a deployable ramp, not to be confused with the inlet ramp, mounted at the exit of the channel. This ramp begins flat to the ground until a fully started flow develops, then raises to a predetermined angle to initiate unstart. They determined that the ramp deployment time had no noticeable effect on unstart time but, alternatively, the ramp deployment angle did have an effect [7]. The ramp angle this paper examines is 26 degrees, as it is the lowest ramp angle seen to induce unstart in the experimental model. This means the computational model can be tuned to unstart precisely at this same angle, allowing for the closest comparability between computational and experimental results.

IV. Developing Inflow Conditions

Demonstrating this experiment of scramjet unstart in a computational model is important for two reasons. First, it validates the code used to simulate unstart, enabling further computational experiments to be conducted with confidence. Second, if the observed flow phenomena can be replicated, then the finer details of the flow can be explored, leading to a greater understanding of the underlying physics. The experiment is limited by the physical constraints of the systems and the observation tools, whereas a computational system is not. Thus, the goal is to replicate the findings of the UT Austin experiment while, simultaneously, gaining a deeper understanding of what is going on during unstart under these conditions.

Several meshes was generated using Pointwise [9] to mimic the inlet-isolator designed in the UT Austin experiment. First, three meshes of various grid spacings were created to simulate a flat plate boundary layer development. This flat plate mesh represents the Mach 5 wind tunnel that the inlet-isolator test section is mounted in. It was necessary to develop the flow first in this domain in order to generate the correct height boundary flow to impose as the inlet condition on the inlet-isolator model.

The medium mesh is shown in Fig. 2 as a representative example. The domains created to generate the flat plate boundary layer were created using a reference length of 1 m, and the grids measured 2 m by 5 m—an order of magnitude larger than the size of the test section—to ensure a fully developed boundary layer. Note that the first 0.5 m of the lower surface is a slip wall, so that the boundary layer trips and begins to develop when it reaches the no-slip wall condition at $x = 0.5$ m. The left hand boundary at $x = 0.0$ m is a Mach 4.9 inlet, with the freestream conditions matching those found experimentally. The upper and right hand wall are outlets. The three grids were 218,450 points, 490,875 points, and 873,800 points, respectively. Note that there is grid clustering in the boundary layer and near the slip to no-slip transition to ensure that the flow is fully resolved.

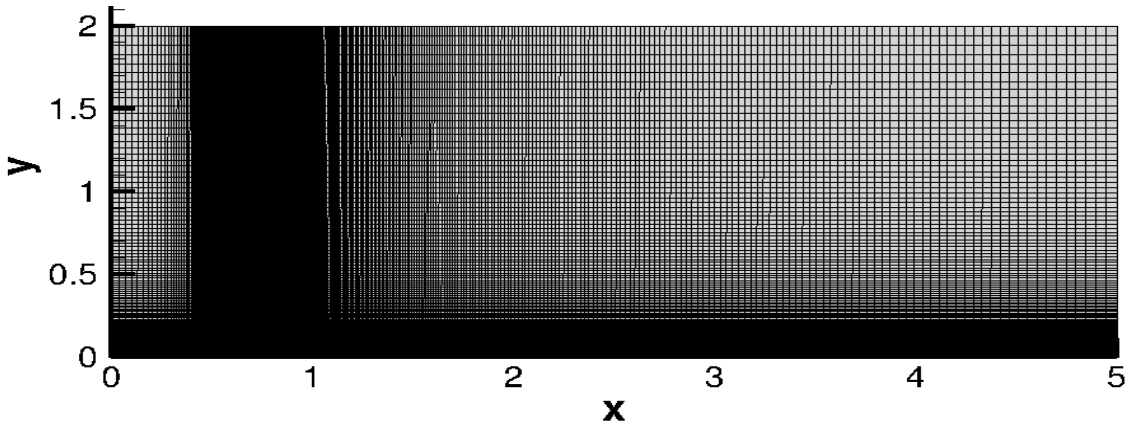

Fig. 2 Flat Plate Mesh

To simulate the flat plate, and later the inlet-isolator model, the SU2 code [10] was used. Using SU2, an open source CFD code developed at Stanford, the high speed flow can be resolved and studied. For this particular investigation, the source code was modified to enable some of the necessary flow field modifications, specifically to impose the flat plate boundary layer on the inlet-isolator model, and to model the ramp deployment for initiating unstart. In addition, to complete the simulation, the computational resources of Purdue University were utilized. The flowfields developed in this study were generated using an unsteady Reynolds-Averaged Navier-Stokes (URANS) flow model. Simulating the flow using a high-order, global time-stepping model, the flow was run with the Spalart-Allmaras turbulence model to best represent the channel flow path and disturbances.

Convergence of the flat plate was determined by looking at the skin friction coefficient at the wall and comparing it to the value predicted by the Van Driest formulation [11]. The skin friction coefficients of all three grids matched closely with each other, as can be seen in Fig. 3, after some minor variations at the leftmost portion of the domain. Furthermore, they match closely with predicted flat plate skin friction coefficients.

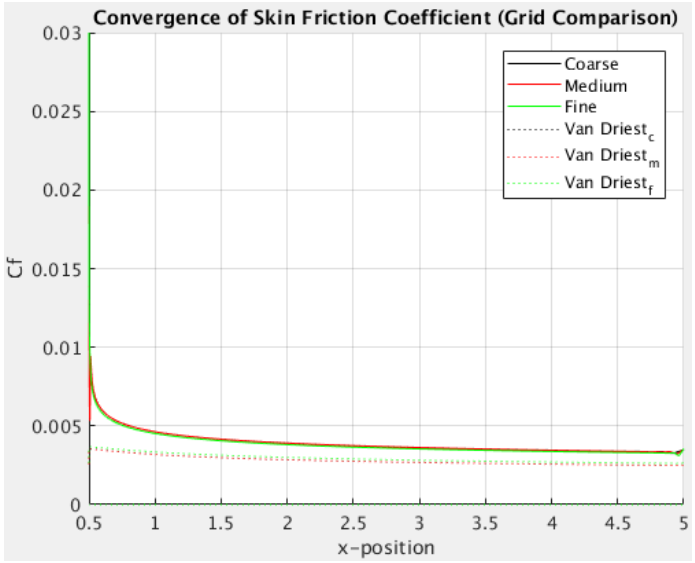

Fig. 3 Grid Convergence Analysis (Flat Plate)

The solution flows from the three meshes were compared to each other in order to verify grid independence of the solution. Note that the grids were clustered at the boundary layer with a $\Delta y+$ value of around 0.1 at the wall. Richardson extrapolation was used for this study of the different grids. The method of calculating the appropriate variables was completed in accordance with the method proposed by Roache et al. [12]. Looking first at the skin friction coefficient, the predicted Richardson value is $C_{f\text{-RICH}} = 0.0032648$. This value has an expected error of 0.066572%, based on the two finest grids. It is in the asymptotic range of convergence, with an asymptotic value of 0.96379. Looking next at the pressure along the wall, the Richardson Extrapolated Pressure at the location where we are extracting the boundary

layer is: P_{RICH} = 5412.8 Pa, with an error band of 0.32290%. Moreover, the solution is in the asymptotic range of convergence with an asymptotic value of 0.99781.

The full, converged solution of the flat plate boundary layer can be seen below, in Fig. 4a. Note that conservative_2 is ρu, or x-velocity multiplied by density. Zooming in at the x-location where the correct boundary layer height is located gives the flow field shown in Fig. 4b. Note that the colored velocity profiles in Fig. 4b are for the velocities within the boundary layer only. The streamwise velocity that is greater than 99% of the freestream velocity is grayed out. Tecplot [13] was used to visualize the results.

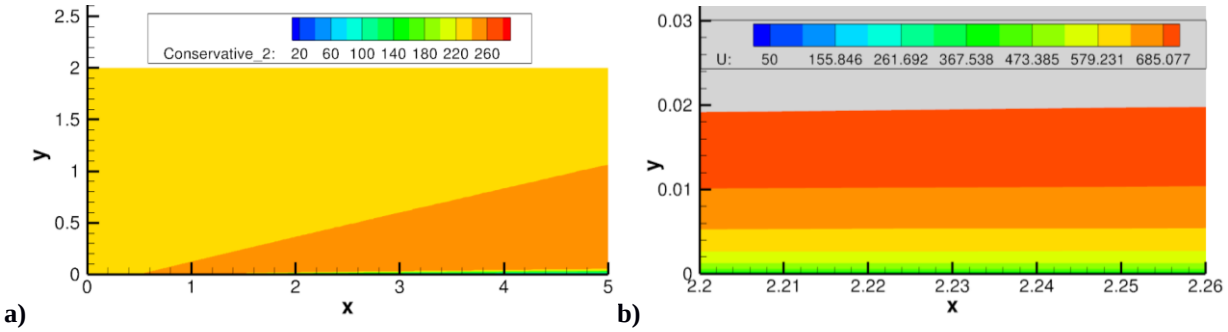

Fig. 4 Flat Plate Boundary Layer Converged Solution: a) Full Mesh Solution, b) Target Boundary Layer Thickness Location

V. Fully Started Solution

An expanded mesh from baseline inlet-isolator geometry was created to ensure that the flow at the inlet and exit are fully developed and not interfered with by grid constraints or imposed/inviolable boundary conditions. The extended mesh can be seen below in Fig. 5. This mesh is scaled based on the flat plate mesh scaling and, similarly, three meshes were created. The coarse, medium, and fine meshes are 90,128 points, 123,228 points, and 215,812 points, respectively. The results shown in the next two sections are for the fine mesh calculations, but the two less resolved meshes gave similar solutions.

Note that when the flow field results are discussed further in this paper, only the experimentally relevant portion of the test section will be shown, as the results preceding the test section inlet (from x = -0.1 m to x = 0 m) and the results downstream of the test section exit (from x = 0.333 m to x = 0.5 m) are not relevant for comparison to experiment. The mesh is set up with supersonic inlet and outlet conditions, and the flat plate boundary layer previously developed is imposed at the inlet.

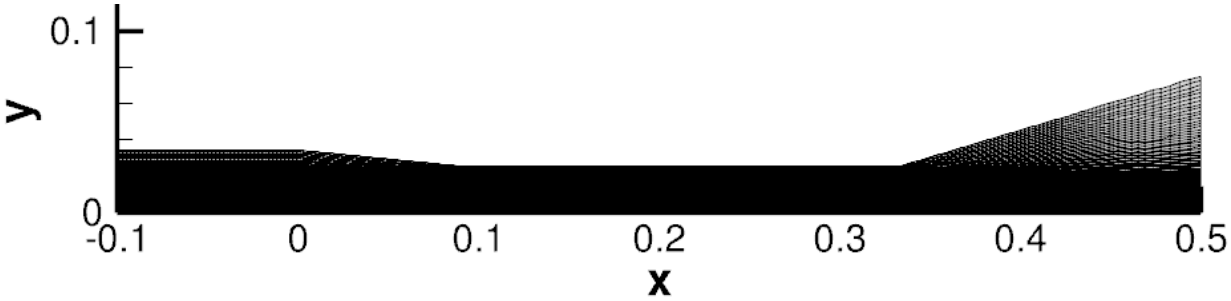

Fig. 5 Inlet-Isolator Mesh (Expanded Geometry)

The baseline flow solution of the inlet-isolator shows the internal shock system of the fully started flow before unstart. The Mach 4.9 flow and large floor boundary layer have entered the inlet-isolator and a shock train develops. In the experiments done at UT Austin, four reflected shocks are found, but the first shock, which emanates from the inlet ramp, is blocked by the nature of the experimental equipment (there is no window in the inlet portion of the test section). Thus, a shock 0 is obscured and only shocks 1, 2, and 3 can be seen, as the view window only encompasses the rectangular isolator portion of the test section. These experimental results are reproduced with permission in Fig. 6.

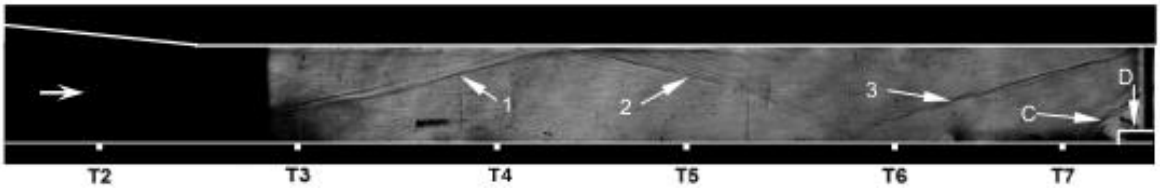

Fig. 6 Experimental Schlieren Image of Fully Started Supersonic Flow, used with permission [6]

In the computational results, all four shocks can be seen. A pseudo-Schlieren image was created and is shown below in Fig. 7, with all four shocks clearly visible. As noted in by Wagner, a thickening of the boundary layer can be seen at the location where shock 1 impinges against the ceiling of the isolator [7]. The location of the four shocks within the inlet-isolator test section match well with the experimental results and show an enhanced image of what is transpiring prior to unstart. Note that the x and y values are non-dimensionalized by the height of the isolator. In addition to the shocks, expansion fans can be clearly seen next to each shock, influencing the boundary layer.

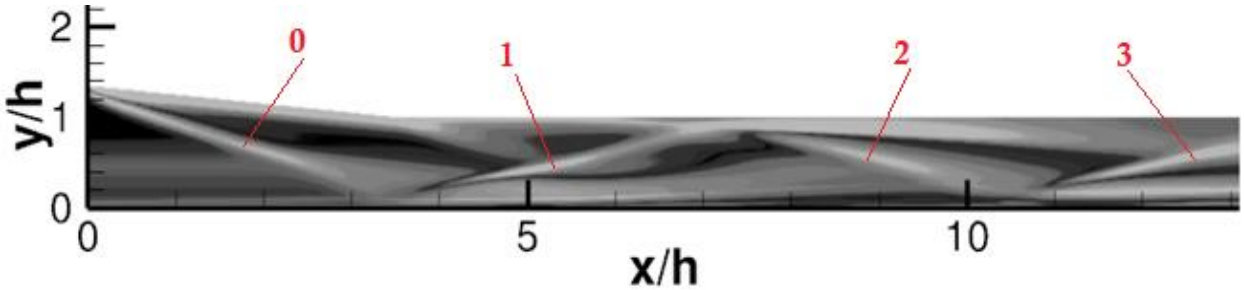

Fig. 7 Computational Pseudo-Schlieren Image of Fully Started Supersonic Flow

The pressures along the floor of the test section were plotted and compared to the values measured at UT Austin. As can be seen below in Fig. 8, the normalized pressures match closely with the values generated by computational methods. There is some variation that can be accounted for by the fact that the experimental state was highly dynamic, but no error bars are given for the experimental data. The same general trends of the pressure are observed, with the pressure increasing rapidly as the flow passes through oblique shocks, and the pressure dropping as the flow passes through reflected expansion fans. The interaction between the wall turbulent boundary layer and the shocks seems to play a large role in the pressure fluctuations.

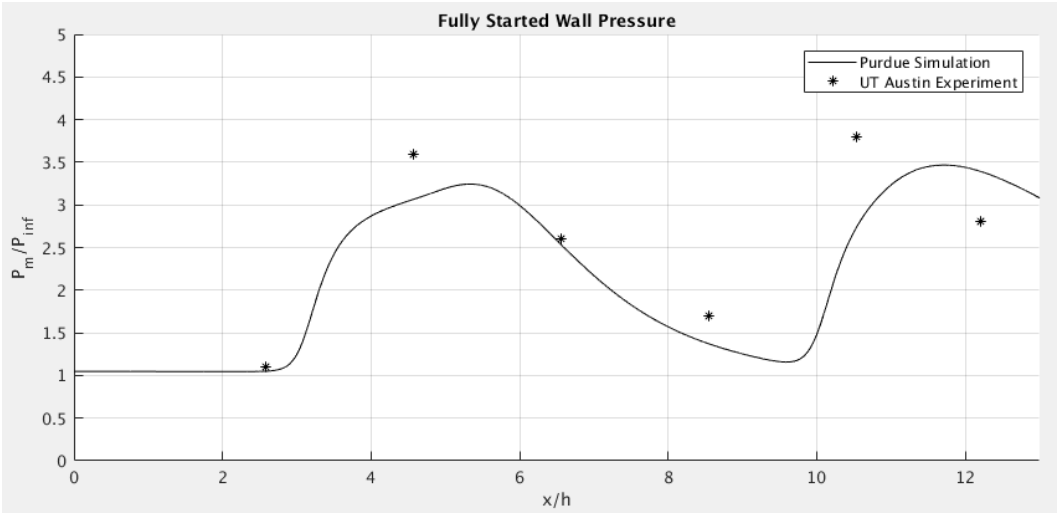

Fig. 8 Normalized Wall Pressure of Pre-Unstart Flow

Wagner et al. also created PIV images of the experimental runs, which have been reproduced with permission below in Fig. 9a. They are compared side-by-side with computational results of the study conducted for this paper. The values shown in the three plots from top to bottom are V (y-velocity), U (x-velocity), and M (Mach number).

Note that the computational images on the right are zoomed in to the portion of the test section that the experiments were able to capture. These results match well and indicate that the computational method used in this study is able to accurately predict the fully started supersonic flow in the inlet-isolator. This gives confidence to the unstart explorations that take place in the following section.

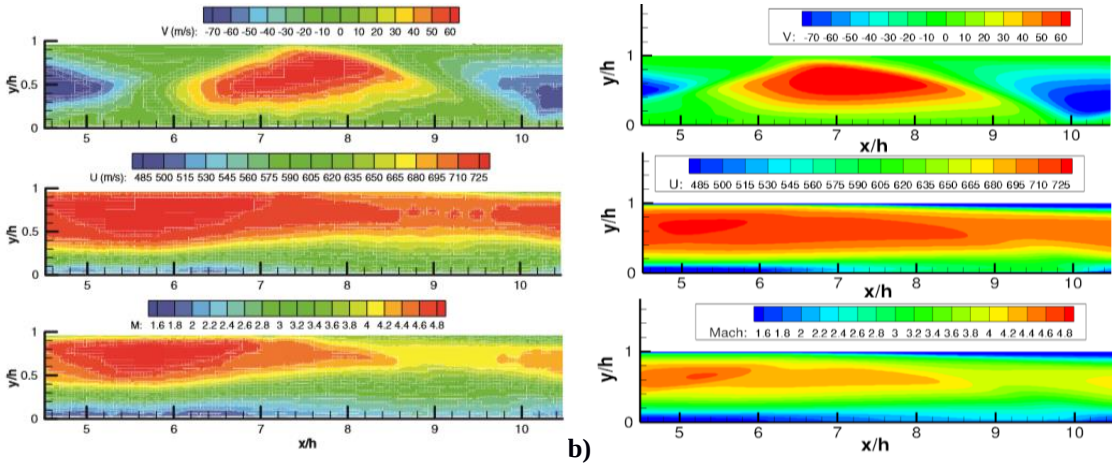

a) b)

Fig. 9 Flow Velocity Contours and Mach Numbers of Flow field: a) Experimental PIV Values, used with permission [8], b) Computational Results

VI. Inlet Unstart

To simulate the inlet unstart, a time accurate model was developed, using a time steps of 1μs. To simulate the deployable ramp at the isolator exit that the experimenters used to induce unstart, an artificial body force was created. The use of the body force obviated the need for a moving mesh, thus greatly simplifying the computations. This body force was implemented as an elliptical in space force distribution, as specified by Atkinson el al. [14]. When initiated, the source term begins flat against the floor of the channel, with the major axis of the ellipse parallel to the x-axis. It is centered at the location in the domain that corresponds to that of the experimental ramp, at the isolator exit. This elliptical source term force is then rotated up, over a period of 1 ms, such that the major axis is aligned to the full ramp angle of 26 degrees. The virtual ramp disrupts the flow and triggers the propagation of a shock back through the supersonic core of the flow, upstream towards the inlet. As can be seen in Fig. 10 below, a high pressure shock develops and propagates toward the inlet. Several different ramp rise times were tested and, as in the experiments, the ramp rise time did not affect the unstart timing or development. Note that the mesh used to study unstart in this section is the same as the mesh used in the previous section, showing the fully started flow.

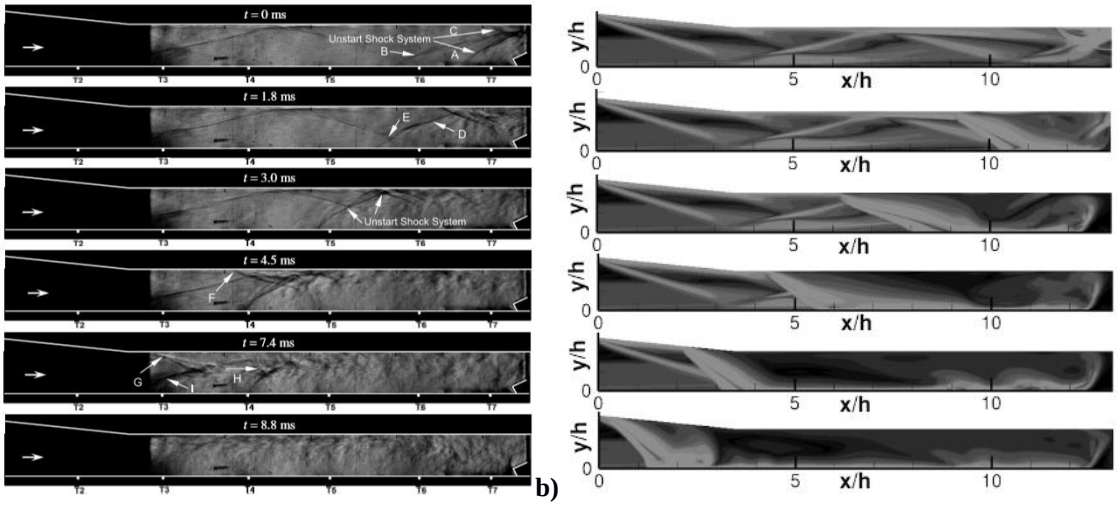

a) b)

Fig. 10 Unstart Process: a) Experimental Schlieren Images, used with permission [6], b) Computational Pseudo-Schlieren Images

The unstart phenomenon in the computational domain matches the experimental unstart fairly closely. The notable features in the flow field, as depicted in the comparative images in Fig. 10, show the shock train being disrupted by an angled unstart shock system, with the shock line running roughly perpendicular to the ramp angle. A more nuanced view of the unstart process is shown when the pressure is investigated. The unstart sequence depicted in Fig. 11 shows how the pressure changes as the unstart shock system propagates towards the inlet. Note that the pressure was normalized by the freestream pressure.

The unstart process begins with a high pressure region initiated by the ramp deployment, as the flow becomes choked at the exit to the isolator. In the fully started portion of the flowfield, there exist regions of slightly higher normalized pressure, which exist due to the shock train and expansion fans. However, these regions exhibit pressure on the order of one to three times that of the freestream flow. The high pressure region that develops as a consequence of the ramp deployment measures on the order of eight to ten times higher than the freestream pressure. This high pressure region is angled in favor of the ceiling of the channel, likely due to the ramp position and the thinner boundary layer present there. As the unstarting region expands upstream, it destroys the more minor pressure variations that existed in the flow. Interestingly, when the high pressure unstart system reaches these minor high pressure regions that exist in the started flow, the interaction between the boundary layer and the high pressure unstart region produces ripples of even higher pressure that propagate downstream, opposite the direction of the unstart system. These pulses can get as high as 30 times the freestream pressure. Note that these pressure pulses rapidly dissipate and do not noticeably affect the unstart process.

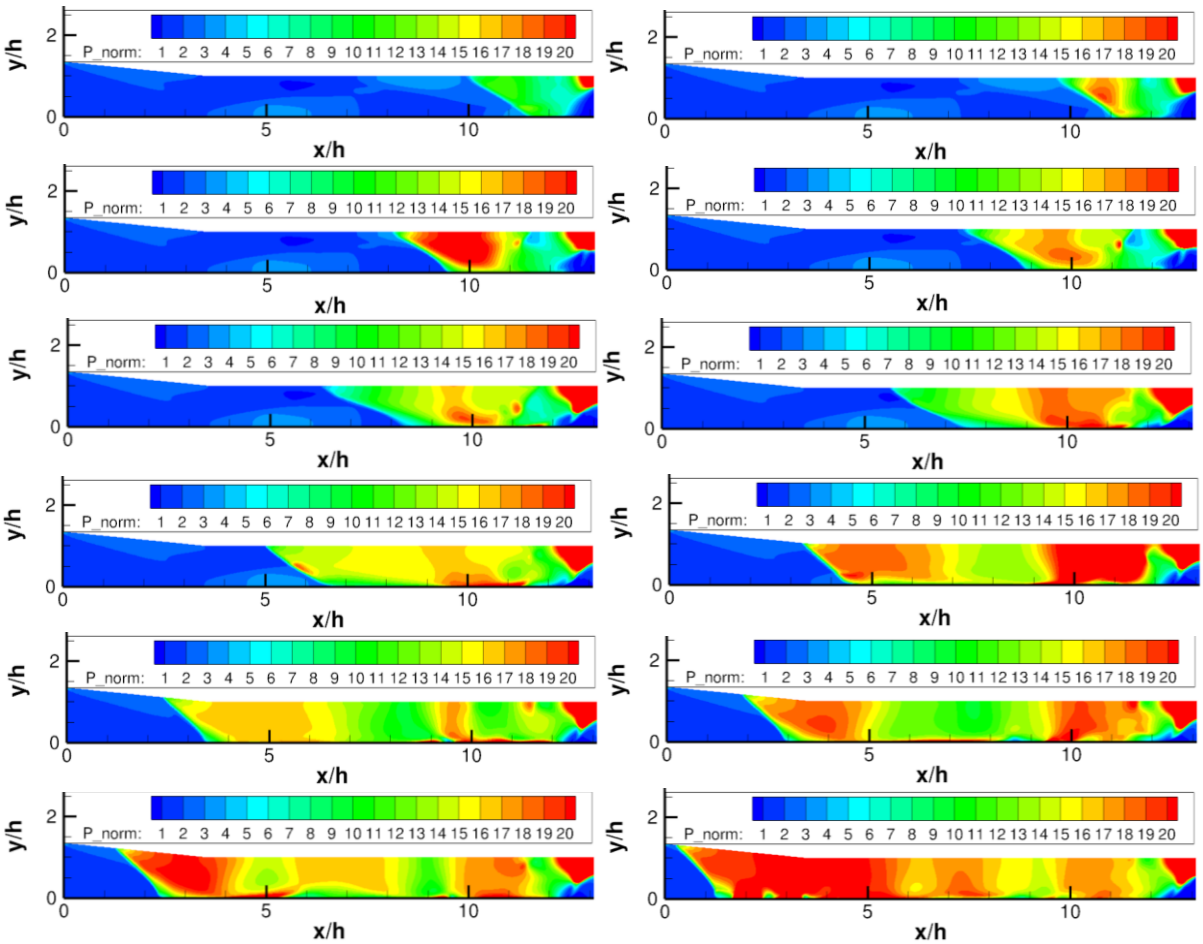

Fig. 11 Unstart Process showing Normalized Pressure Rise

Once the furthest upstream part of the pressure wave travels 242.3 mm upstream through the isolator, it reaches the inlet portion of the test section. At this point, the throat area opens up due to the inlet ramp for the remaining 90.7 mm of the channel and the unstart process changes. At this point, the high pressure region near the ceiling of the test section slows while, simultaneously, the region near the floor of the channel continues along at the same speed. This

causes the sharp angle of the shock to change, leading to a curved shock front. As this happens, the pressure downstream of the shock, contained within the unstart system, increases again. This time, the pressure rise is sustained, and a normalized pressure on the order of 30 times the freestream propagates downstream through the entire unstarted region of the channel.

Investigating the flow Mach number also helps elucidate the major features of the unstart flow. Seen below, in Fig. 11, the flow starts fully supersonic except for the thin boundary layers on the top and bottom walls of the channel. Note that, prior to unstart, the core of the flow, in the center of the channel, has the highest velocity. However, for the purposes of exploring the unstart process, the images in Fig. 11 have been limited to showing a maximum flow velocity of Mach 1. This limitation gives a more detailed view of the unstart system itself.

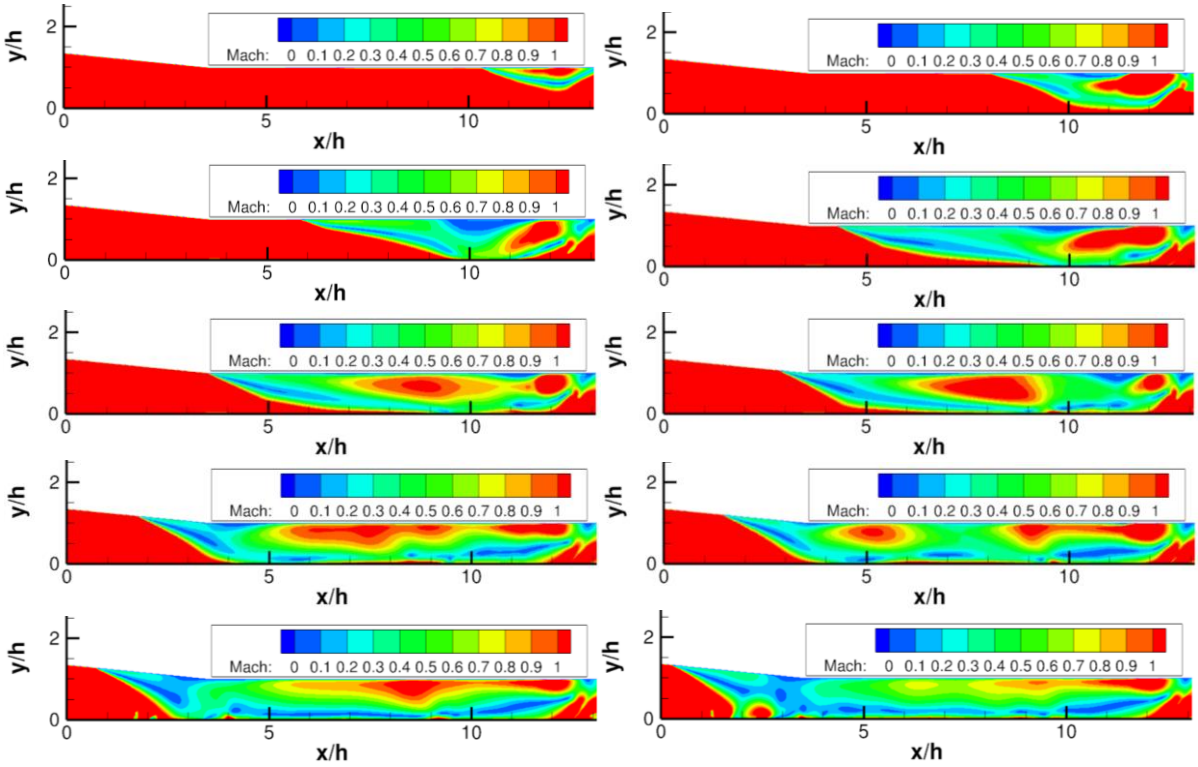

Fig. 11 Unstart Process showing Flow transitioning to Subsonic

When unstart is initiated, a region of subsonic flow develops, with a similar shape and location to the pressure wave previously shown. The core supersonic flow becomes subsonic as the unstart process propagates upstream, eventually leading to fully subsonic flow in the entire inlet-isolator test section. It is observed, however, that in the same locations of thick boundary layer that caused pressure spikes, spikes in the Mach number are happening as well. This causes pulses of higher velocity flow to develop and dissipate as the unstart wave reaches each shock impingement location from the fully started flow.

VII. Precursors to Unstart

The pressure distribution along the top and bottom walls of the channel was investigated to determine if a precursor to unstart was present. Should a sudden pressure change be seen in the wall boundary prior to the unstart system reaching it, it could indicate that pressure is an effective way to detect unstart. The change in wall pressure as unstart progresses is displayed in Fig. 12. The fully started pressure distribution of any given point in the channel remains almost constant during the simulation until the high pressure unstart region reaches it. It should be noted that unstart is happening roughly twice as fast in this simulation as in the experiments conducted at UT Austin, but the associated phenomena are the same. The pressure rise from unstart on both the top and bottom walls is significantly larger than the mean pressure distribution. The pressure rise along the top surface of the channel stabilizes within the unstart system to roughly 20 times the freestream pressure, similar to that seen by Wagner et al. [6]. The bottom wall sees much larger pressures, on the order of 90 times the freestream pressure. Furthermore, the pressure along the floor of the channel is much less uniform during unstart than that on the bottom wall.

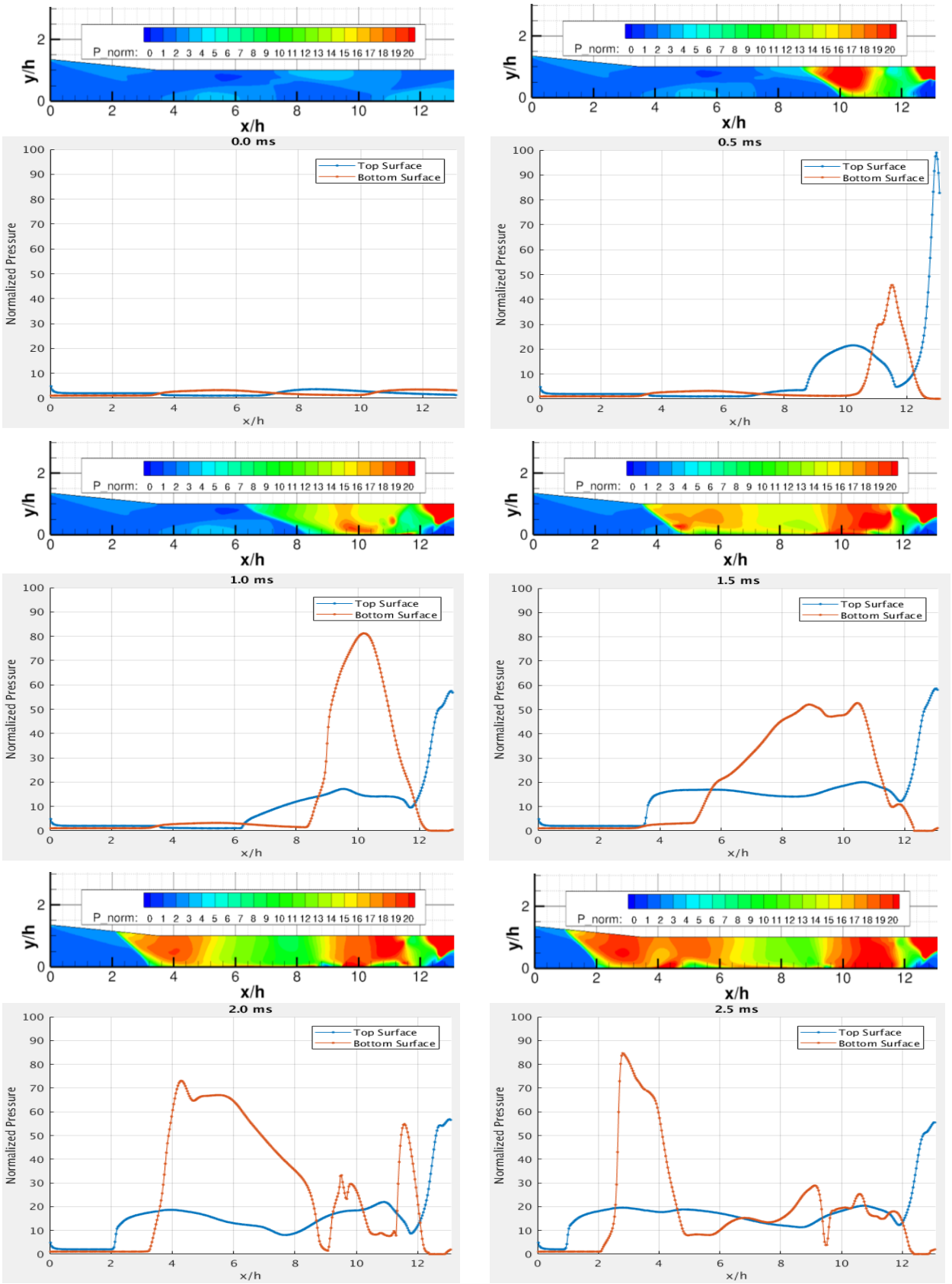

Fig. 12 Wall Pressure Traces during Unstart at 0.0 ms, 0.5 ms, 1.0 ms, 1.5 ms, 2.0 ms, and 2.5 ms

In this two-dimensional case, with the given resolution, very little indication of unstart can be detected in the pressure inside the wall boundary layer of the inlet-isolator. However, looking at the pressure difference along the wall, gives an indication that an unstart precursor may be present in the boundary layer. Fig. 13 shows the difference between the normalized unstarted pressure and the fully started flow pressure along the top and bottom walls, as unstart progresses.

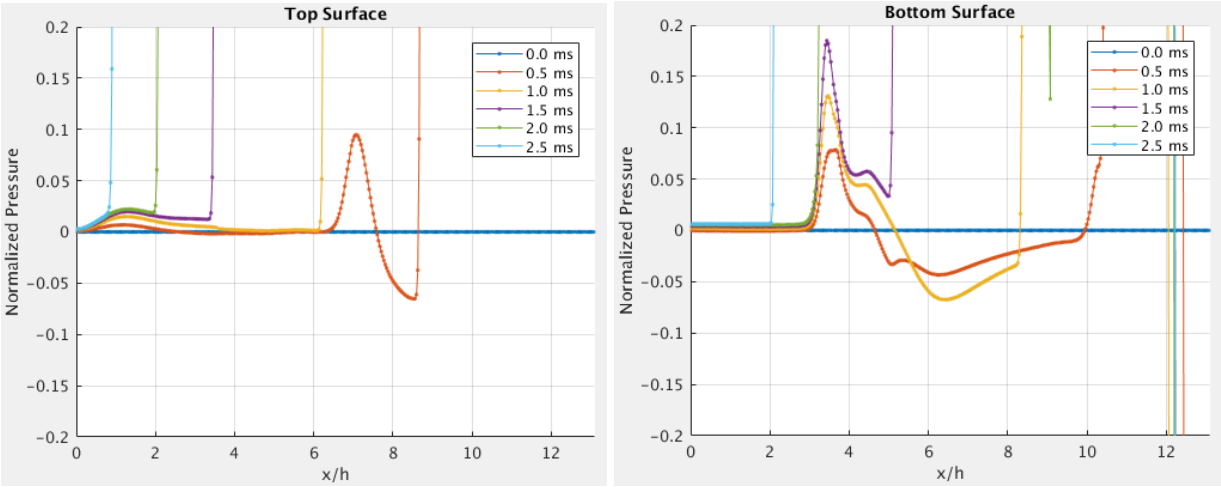

Fig. 13 Wall Pressure Differential during Unstart

Pressure fluctuations can be seen along the top and bottom walls of the channel upstream of the unstart shock system. The strength of these fluctuations, which measure up to approximately 20% of the fully started pressure, grow as the unstart shock approaches, until they are consumed by the unstart pressure wave. The boundary layer is the only subsonic region of the flow outside the unstart system, and thus is the only region that could potentially carry downstream information back upstream. The pressure fluctuations on the bottom surface are several times larger than those on the top surface, likely due to the significantly larger boundary layer present along the bottom wall.

These roughly Gaussian distributions of pressure change that exist upstream of the unstart shock system are located at key points in the channel. Along the top surface, they are positioned at approximately x/h = 1.5 and x/h = 7, and along the bottom surface, they are located primarily at x/h = 3.5. Looking back at Fig. 7, the locations x/h = 7 is where shock 1 reflects off the top wall and x/h = 3.5 is where shock 0 reflects off the bottom wall. The precursor pressure pulse locations and the shock impingement locations appear to be linked. The pulse at x/h = 1.5 could be due to the expansion fan from shock 0 and the constricting throat from the inlet ramp, but requires further study. It is possible that there could be another pressure pulse location within the floor boundary layer at x/h = 10.5, where shock 2 intersects the floor of the channel, but it is too close to the initial unstart location to resolve in this study.

VIII. Conclusions

This paper demonstrates that a fully started hypersonic flow can be accurately modeled in an inlet-isolator geometry. Different boundary layers can be developed to match experimental conditions as needed and the major flow features can be resolved. In addition, the unstart process can be modeled with reasonable accuracy, although the timing of the flow disruption is accelerated in the computational model. Interactions between the shock train, unstart pressure rise, and wall boundary layers have been observed and suggest a complex, coupled dynamic.

This paper shows the ability of a body force, specifically an elliptical source term, to create accurate unstart conditions. Using a body force eliminates the need for a moving mesh, which drastically simplifies the computations needed to demonstrate unstart. This simplification will enable much higher fidelity calculations to be made in a similar time as previous moving mesh calculations.

Precursors to unstart have been explored, and pressure pulses in the top and bottom wall boundary layers have been found that may be indicators of unstart. These pulses of high pressure appear at the locations of fully started flow shock impingement, preceding the unstart system. As the high pressure unstart region approaches these locations, the pressures pulses grow until they are destroyed by the unstart shock front. Further study is required, but this provides a promising avenue for future work, both for identifying unstart precursors and their expected locations.

The simulations shown in this paper are all in two dimensions, so they neglect the incorporation of three dimensional effects, such as the corner flows and reflections in multiple directions. Future work will need to reproduce

these findings in three dimensions, to achieve an even closer representation of the unstart process. This will enable a deeper study into the possible precursors to unstart, which appear to precede the unstart shock system in the boundary layer. If these can be investigated more thoroughly and verified, technology can be developed and deployed, such that the flow is disrupted when unstart begins, stopping the shock train from reaching all the way to the inlet, which could lead to consistent and stable hypersonic flight.

Acknowledgements

I. Hall received support under the DoD SMART Scholarship program. Computer time for this work was provided by Purdue University. The authors would also like to thank Noel Clemens and Justin Wagner for their permission to reproduce several of their figures in this paper.

References

[1] Barber, T. A., Maicke, B. A., and Majdalani, J., "Current State of High Speed Propulsion: Gaps, Obstacles and Technological Challenges in Hypersonic Applications", AIAA Paper 2009-5118, Aug. 2009.
[2] Waltrup, P. J., White, M. E., Zarlingo, F., and Gravlin, E. S., "History of U.S. Navy Ramjet, Scramjet, and Mixed-Cycle Propulsion Development", Journal of Propulsion and Power, Vol. 18, No. 1 (2002), pp. 14-27.
[3] Curran, E. T., and Stull, F. D.., "The Utilization of Supersonic Combustion Ramjet Systems at Low Mach Numbers", AF Aero Propulsion Laboratory, RTD-TDR-63-4097, Wright-Patterson Air Force Base, Ohio, Jan 1964.
[4] Adams, J. C., Martindale, W. R., and Varner, M. O., "One-Dimensional Unsteady Modeling of Supersonic Inlet Unstart/Restart", January 1984, AIAA Paper 1984-0439.
[5] Wagner, J. L., Valdivia, A., Yuceil, K. B., Clemens, N. T., and Dolling, D. S., "An Experimental Investigation of Supersonic Inlet Unstart", AIAA Paper 2007-4352, June 2007.
[6] Wagner, J. L., Valdivia, A., Yuceil, K. B., Clemens, N. T., and Dolling, D. S., "Experimental Investigation of Unstart in an Inlet/Isolator Model in Mach 5 Flow", AIAA Journal, Vol. 47, No. 6 (2009), pp. 1528-1542.
[7] Wagner, J. L., "Experimental Studies of Unstart Dynamics in Inlet/Isolator Configurations in a Mach 5 Flow", Ph.D. Thesis, Univ. of Texas, Austin, TX, 2009.
[8] Wagner, J. L., Yuceil, K. B., and Clemens, N. T., "Velocimetry Measurements of Unstart in an Inlet-Isolator Model in Mach 5 Flow", AIAA Journal, Vol. 48, No. 9 (2010), pp. 1875-1888.
[9] Pointwise, Software Package, Ver. 18.0, Pointwise, Inc., Fort Worth, TX, 2018.
[10] SU2, Software Package, Ver. 5.0, Stanford University, Palo Alto, CA, 2018.
[11] E. R. Van Driest. Turbulent boundary layer in compressible fluids. Journal of the Aeronautical Sciences, 18(3):145–160, 1951
[12] Roache PJ. Perspective: A Method for Uniform Reporting of Grid Refinement Studies. ASME. J. Fluids Eng. 1994;116(3):405-413.
[13] Tecplot 360 EX, Software Package, Ver. R1, Tecplot, Inc., Bellevue, WA, 2018.
[14] Atkinson, M., Poggie, J., and Camberos, J., "Control of High-Angle-of-Attack Reentry Flow with Plasma Actuators", Journal of Spacecraft and Rockets, Vol. 50, No. 2 (2013), pp. 337-346.